On the sensitivity of seasonal and diurnal precipitation to cumulus parameterization over CORDEX-EA-II

Xiaorui Niu[1,2,3] · Jianping Tang[1,2] · Shuyu Wang[1,2] · Congbin Fu[1,2] · Deliang Chen[3]

Abstract

The ability of the Weather Research and Forecasting (WRF) model in simulating the seasonal and diurnal cycles of rainfall over the Coordinated Regional Climate Downscaling Experiment East Asia Phase II (CORDEX-EA-II) domain is validated against the Tropical Rainfall Measuring Mission (TRMM) datasets. A focus is placed on the role of convective parameterization (CP) schemes. A set of numerical experiments at a 25 km resolution for 1998–2009, using six different CPs, is performed to evaluate the physics-dependency of simulation results. All CPs simulate realistic summer mean precipitation and its northward propagation, with the best performance in the Simplified Arakawa-Schubert (SAS). The biases in the seasonal evolution of rainfall are related to the deficiency in simulated low-level winds and the northward propagation of the cyclonic vorticity. The simulated earlier peak time in other CPs is delayed by about 1–2 h by the Kain-Fritsch with a modified trigger function (KFMT), although this scheme shows a disadvantage in the magnitude. The performance of different CPs in simulating diurnal rainfall cycles is dependent on regions, and none of them performs better than the others for all the sub-regions. The initiation of simulated convection is weakly physics-dependent. However, the timing and magnitude of stratiform precipitation differ among the six experiments. A further analysis shows that the dry biases over the lower Yangtze River basin are a result of the weakened southwesterly water vapor transport, while the excessive afternoon rainfall in the Kain-Fritsch (KF) simulation is attributed to the largest positive perturbation in the lower level atmosphere, especially the enhanced vertical transport of humidity.

Keywords WRF regional model · Convective parameterization schemes · Stratiform precipitation · Convective precipitation · CORDEX-EA-II

✉ Jianping Tang
jptang@nju.edu.cn

1   Institute for Climate and Global Change Research, School of Atmospheric Sciences, Nanjing University, Nanjing, China

2   Jiangsu Collaborative Innovation Center for Climate Change, Nanjing, China

3   Regional Climate Group, Department of Earth Sciences, University of Gothenburg, Gothenburg, Sweden

1 Introduction

As a major component of the global climate system, the East Asian summer monsoon (EASM) has a profound influence on the lives of roughly one-fourth of the world's population (Ding and Chan 2005). Due to its unique orographic forcing, EASM is characterized by complex spatial and temporal variabilities, which provide an ideal test-bed for evaluating model performance and assessing the sensitivity of different types of parameterizations (Lau et al. 1988; Yu et al. 2007; Zhou et al. 2008).

One of the prominent features of EASM rainfall is its north–south shift, with two abrupt northward jumps and three stationary periods (Lau et al. 1988; Ding and Chan 2005). The diurnal cycle of precipitation (DCP) is another important aspect in EASM variability and has been a hot issue (Yin et al. 2009), as it is intimately connected with thermal variations, local circulations, moisture convections,

and boundary-layer development (Dai et al. 1999; He and Zhang 2010; Yuan et al. 2012). The observed summer precipitation over East Asia is featured by distinct diurnal variation, with considerable regional features and an eastward phase delayed in the peak time of precipitation along the Yangtze River Basin (YRB) (Yu et al. 2007; Zhou et al. 2008; Chen et al. 2018). Hence, the depictions of those two features in the model constitute major metrics to assess model performance, and are also useful to enhance understanding of the physical mechanisms involved in EASM processes. However, it is still a challenge for state-of-the-art climate model to satisfactorily reproduce the observed features, especially for DCP over East Asia (Zhang and Chen 2016; Yang et al. 2018).

The regional climate model (RCM), with refined grid spacing and solid model physics, has been widely used to generate regional climate information and understand the regional-scale processes (Leung et al. 2004; Fu et al. 2005; Giorgi and Lionello 2007). Previous studies mainly focus on the climatological mean state, demonstrating that RCMs do indeed show advantage over global climate models (GCMs) in reproducing local to regional climate properties (Gao et al. 2012; Niu et al. 2015a, b; Zou and Zhou 2016). While for DCP, most RCMs could broadly reproduce the observed DCP and even regional characteristics, but still have large deficiencies in diurnal timing, as well as the frequency and intensity of precipitation (Kang and Hong 2008; Walther et al. 2013; Jin et al. 2016; Gao et al. 2017). Typically, RCMs usually advance the time of the maximum precipitation and display an unrealistically large diurnal range over land areas (Dai 2006; Choi et al. 2015; Li et al. 2018). They also fail to satisfactorily reproduce the observed propagating signals over the eastern slope of elevated land areas (Liang et al. 2004a; Gao et al. 2017).

Precipitation is commonly modeled as the composition of stratiform precipitation and convective precipitation, with the latter generated by the cumulus parameterization scheme (referred to as CP in the following text), which is the main error source of the simulated precipitation (Koo and Hong 2010). Therefore, the choice of CP in models affects not only the occurrence and amount of precipitation, but also the onset timing and location (Gao et al. 2017). In particular, CP is the most important trigger in simulating DCP over land, as DCP is highly dependent on convection activity (Bechtold et al. 2004; Koo and Hong 2010; Gianotti et al. 2012). Previous researches have documented the sensitivity of simulated DCP to CP over various regions. For example, He et al. (2015) evaluate three CPs in the Regional Spectral Model (RSM) over West Africa at two horizontal resolutions, and point out that CPs mainly affect the amplitude of the diurnal cycle and the partitioning between convective and stratiform, but insignificantly affect the phase. Identifying simulations with

twelve popular CPs, Qiao and Liang (2015) reveal that the Grell scheme performs better in reproducing the Central United States diurnal amplitude, phase, and nocturnal rainfall maxima than others. Some components in CP such as closure, entrainment, and the triggering function, have been modified to improve the simulation of DCP, and encouraging results have been produced (Liang et al. 2004a; Bechtold et al. 2014; Folkins et al. 2014).

To provide a coordinated model evaluation framework and generate improved regional climate information necessary for vulnerability, impact, and adaptation studies, the Coordinated Regional Climate Downscaling Experiment (CORDEX) was initiated by the World Climate Research Programme (WCRP) in 2009 (Giorgi et al. 2009). It is now underway to move forward into its second phase (CORDEX-II) due to the development of RCMs and the demand for higher resolution. As the East-Asian branch of the CORDEX initiative, the second phase of CORDEX-East Asia (CORDEX-EA-II) adopts new domain with 0.22°resolution (about 25 km). A number of studies have evaluated the performance of RCMs (Zou and Zhou 2016; Shen et al. 2017; Tang et al. 2017, 2018; Wang et al. 2018) and projected regional climate changes (Wang et al. 2019) over CORDEX-EA Phase I and II domains. In this study, we design six experiments under the framework of the CORDEX-EA-II using the Weather Research and Forecasting (WRF) model (Skamarock and Klemp 2008) to investigate the effects of CPs on the simulated precipitation characteristics over the CORDEX-EA-II domain, in terms of summer mean and DCP. Such a sensitivity experiment has yet to be conducted for long-term simulations over the CORDEX-EA-II, as previous investigations were mainly simulated by GCMs (Chen et al. 2010; Yuan et al. 2013; Zhang and Chen 2015) or carried out for only 1 year or relatively small regions (Jin et al. 2016; Li et al. 2018). The comparisons of model performances in this study will identify the strengths and weaknesses of individual CP, and improve our understanding of how to better simulate DCP over CORDEX-EA-II domain.

The remainder of this paper is organized as follows. Section 2 introduces the model, experimental design, the evaluation data, and the methods. Section 3 presents the comparisons among the observations and simulations, in terms of climatological mean state and diurnal variation, and the possible physical mechanisms leading to differences among the CPs are also discussed. Section 4 offers the main findings and discussion.

2 Model configuration and data descriptions

2.1 Experiment set-up

To evaluate the performance of different CPs, six regional experiments are performed using the WRF model, which has been widely applied in regional climate simulations over East Asia and demonstrates performance well in this region (Shen et al. 2017; Tang et al. 2017, 2018). All simulations are integrated over CORDEX-EA-II domain (Fig. 1) and run for 22 years, with model outputs (rainfall) archived at the six-hour (hourly) timescale for 1988–2009. The
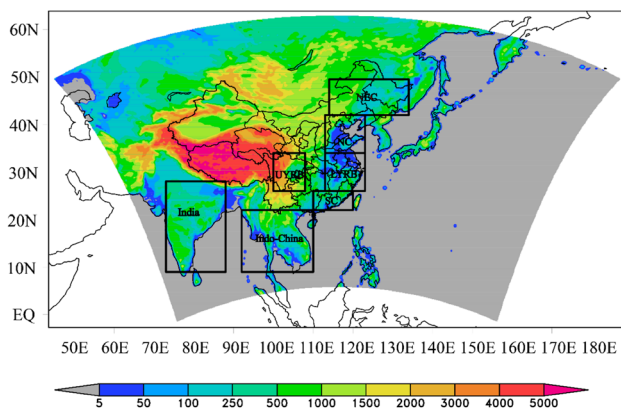
Fig. 1 The simulation domain and topography. East Asia is divided into seven sub-regions based on the distinct diurnal features, including Northeast China (NEC, 42–49.5°N, 114–134°E), North China (NC, 34–42°N, 113–123°E), the upper Yangtze River Basin (UYRB, 26–34°N, 100–108°E), the lower Yangtze River Basin (LYRB, 26–34°N, 113–123°E), South China (SC, 22–26°N, 110–120°E), India (9–28°N, 73–88°E), and Indo-China (9–22°N, 92–110°E)

horizontal resolution of 25 km, with 384 (in west–east) × 252 (in south–north) grid points and 29 sigma levels in vertical direction, are adopted in this study. The initial and boundary conditions are provided every 6 h by ERA-Interim reanalysis data (ERA-IN) at 0.75° × 0.75° resolution (Dee et al. 2011). The sea surface temperature (SST) is prescribed every 6 h from the Optimum Interpolation Sea Surface Temperature (OISST) weekly datasets (Reynolds and Smith 1994).

The main physical options used in this study include the Single-Moment 5-class scheme for microphysics (Lim and Hong 2010), Yonsei University parameterization of the planetary boundary layer (Hong et al. 2006), the Community Atmosphere Model for the longwave and shortwave radiation scheme (Collins et al. 2004), and the NOAH land surface model (Chen and Dudhia 2001). The simulations vary only in CP schemes and with the same option for other physical processes. These different CPs are the Betts-Miller-Janjic (BMJ, Betts and Miller 1986; Janjić 1994), the Kain-Fritsch (KF, Kain and Fritsch 1990), the KF scheme with an alternative trigger function weighted by moisture advection (KFMT, Ma and Tan 2009), the Grell-3D ensemble (GR3D, Grell and Dévényi 2002), the updated version of the Simplified Arakawa-Schubert (SAS, Han and Pan 2011), and the multiscale Kain-Fritsch (MSKF, Zheng et al. 2016). Detailed description of those CPs can be found in Table 1.

2.2 Datasets and methods

To examine the capability of reproducing precipitation climatology and its diurnal cycle, the Tropical Rainfall Measuring Mission (TRMM) 3B42 version7 data, which has been confirmed to be a good measure with reliability and validity for evaluating DCP over East Asia (Zhou et al. 2008; Yuan et al. 2012), is used in this study. The TRMM data are available at 0.25° × 0.25° resolution and represent a

Table 1 Main features of six different cumulus parameterization schemes used in this study

Scheme	Type	Trigger	Closure	Entrainment Formulation
BMJ	Adjustment	CAPE, cloud depth threshold value, and moist sounding needed	Quasi-equilibrium closure	Convection profiles and relaxation time depends on cloud efficiency
KF	Mass-flux	Perturbation based on low-level vertical motion	CAPE closure	Variability of cloud radius and cloud-depth threshold allowed
KFMT	Mass-flux	Perturbation based on local average moisture advection	Same as KF	Same as KF
GR3D	Mass-flux	Trigger function varies for each member	Multi-closure can be based on: CAPE, Moisture convergence, low-level vertical velocity	Height and RH dependent
SAS	Mass-flux	Parcel buoyancy	Quasi-equilibrium closure	Height and RH dependent
MSKF	Mass-flux	Same as KF, but with subgrid-scale effect	Same as KF	Same as KF, but with scale-aware parameterized cloud dynamics

CAPE the convective available potential energy, *RH* means relative humidity

nominal ± 90 min span around the nominal universal coordinated time (UTC) hour. For temporal consistency between TRMM and simulations, the TRMM datasets are interpolated to 1-hourly precipitation on a UTC frame by a cubic spline method. Considering the launched time of TRMM, the results from 1998–2009 are analyzed in this study. Variables including wind, temperature, and specific humidity at 0000UTC, 0600UTC, 1200UTC, and 1800UTC from the ERA-IN are also adopted in this study to evaluate model performance in simulating large-scale circulation and convective activity. In addition, model results are interpolated to a 0.25° × 0.25° latitude–longitude grid over the simulation domain for the convenience of comparison.

Rainfall rate, as well as its frequency and intensity are the main parameters that can be used to describe the characteristics of rainfall. Following Dai (2006), summer mean precipitation amount (PA) is calculated as the accumulated precipitation divided by the total hours in summer, precipitation frequency (PF) is defined as the percentage of the total number of the measurable precipitation (≥ 0.1 mm/h) to the total number of hours in summer, precipitation intensity (PI) is the cumulative hourly precipitation rate divided by the total precipitating hours with the measurable precipitation in summer. The hourly PA, PF, and PI data are computed at each grid for each season and then averaged over all the years within the period of 1998–2009. To investigate

DCP, the results are also converted from the UTC frame to the local solar time (LST) frame based on the longitudinal dependency.

3 Results

3.1 Climatological mean states

Figure 2 depicts the mean summer precipitation over East Asia derived from the TRMM data and the differences between the simulations and observations. The overall precipitation pattern, including the major continental rainbands located on the southern edge of the Tibetan Plateau, in the Indochina peninsula, and over the south of Japan to southern China and the Korean peninsula, is reproduced by all CPs. Although, they all exaggerate oceanic precipitation, especially over the ocean south of 30°N. By examining the differences among the experiments, we find that the underestimated precipitation over eastern China produced by BMJ and GR3D is confined by other CPs. Compared to the results in KF, KFMT can effectively reduce the excessive precipitation over the Indochina Peninsula and western North Pacific, while aggravate the dry biases over northern India. Overall, all the experiments show a better skill over land than ocean, as the spatial correlations (CORR) lie between 0.38 and 0.69

Fig. 2 The observed summer precipitations (**a**) and the difference between the simulated and observed summer precipitation (**b**–**g**) over East Asia during 1998–2009 (unit: mm/d)
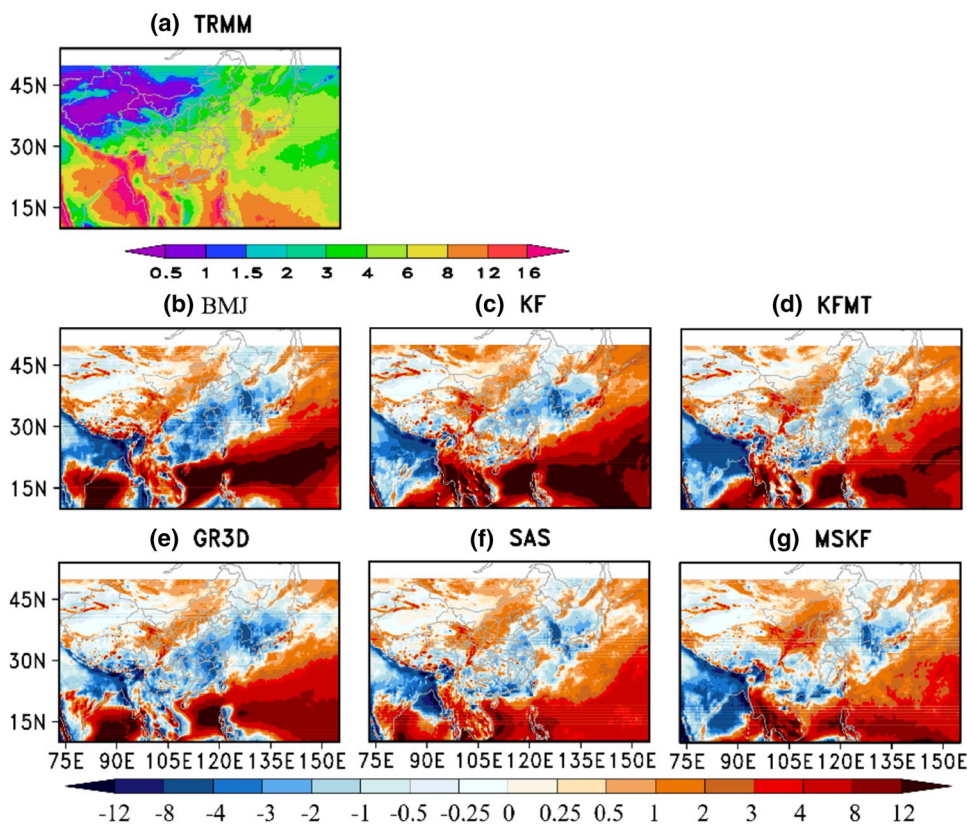
for ocean areas and are above 0.69 for land regions (Table 2). Comparatively, SAS produces a better simulation of summer precipitation over East Asia than other CPs, with a lower bias and root-mean square error (RMSE) and higher CORR, which is consistent with Kang and Hong (2008).

Time-latitude distributions of climatic mean pentad precipitation averaged between 105–123°E are illustrated in Fig. 3. In the observation, the rain belt propagates northward rapidly from the regions about 20–25°N to the area of 25–35°N during the period of the 30th–40th pentad, with values larger than 9 mm/d. Afterwards, it advances northward again reaching North China and Northeast China in the period between the 40th and the 50th pentad. Then, the rain belt rapidly moves back to South China after the 50th pentad. Compared to the observations, all CPs capture the broad migration of the rain belt with the CORRs larger than 0.76. However, large systematic biases exist. In BMJ, KF, and GR3D schemes, obviously stronger precipitation over the regions around 20°N is simulated and the migration of rain belt over the YRB is not well reproduced. The results in KFMT, SAS, and MSKF are more consistent with observations in terms of both the temporal-space migration of the main rain belt and rainfall amount, especially in the SAS scheme which has highest CORR and lowest RMSE. Meanwhile, the rain belt over the YRB spans a shorter time period in most of the CPs compared to the observation. Those biases in time and location, which are also common for simulating the seasonal migration of the East Asian summer moon rain belt in models, result in the precipitation deficiency over East Asia (Fig. 2).

As the seasonal advance and retreat of the summer monsoon in East Asia are closely related to the large-scale

Table 2 The spatial statistical skill scores (Correlation Coefficient (CORR) and Root Mean Square Error (RMSE) associated with the six convection schemes for summer mean PA during 1998–2009 over the whole East Asian domain, as well as land and ocean regions

	BMJ	KF	KFMT	GR3D	SAS	MSKF
CORR						
All	0.53	0.65	0.68	0.71	0.72	0.70
Land	0.72	0.69	0.69	0.77	0.78	0.71
Ocean	0.38	0.56	0.63	0.69	0.63	0.64
RMSE (mm/d)						
All	6.70	7.77	6.26	5.09	3.85	4.48
Land	3.24	5. 81	5.02	3.14	2.80	4.08
Ocean	9.42	9.70	7.54	6.80	4.86	4.94

Fig. 3 Time-latitude cross section of pentad mean precipitation rate averaged between 105°E and 123°E (unit: mm/d): **a** observations, **b**–**g** different CPS
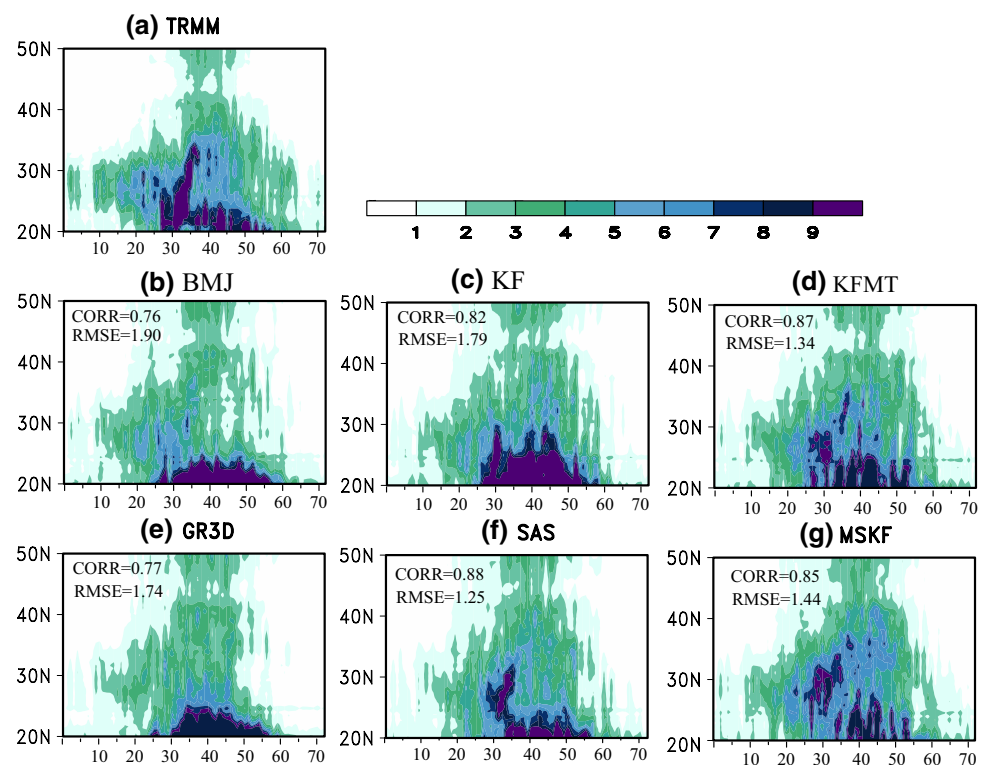
circulation, Fig. 4 shows the time-latitude distributions of the pentad mean 850 hPa wind and vorticity averaged along 105–123°E. From the reanalysis data, the prevailing winds turn from northeasterly to southwesterly around the 25th pentad in the lower latitude domain between 10°N–20°N, suggesting the onset of the summer monsoon over this region. In the following 35th to 42th pentad, the southwesterly moves northward over East Asia with strengthened windspeed and accompanied by the northeastward migration of low-level cyclonic vorticity. Such circulation features lead to the seasonal shift of the rain belt over East Asia.

All CPs reproduce the observed reversal of dominating wind field around 25th pentad over the regions between 10°N–20°N. However, BMJ, KF, and GR3D generate displaced southwesterly flow over Eastern China during the 35–42th pentad. Such deficiency in low-level winds, associated with a weakened northward propagation of the cyclonic vorticity, results in the northward displacement of the rain belt in this area. KFMT, SAS, and MSKF improve the simulation of the southwesterly flow and cyclonic vorticity over subtropics, although the magnitudes are weaker than the observations. Therefore, they show higher skills in simulating the seasonal progression of the rain belt over eastern China.

As the simulation of the circulation and thermobaric structure at low and middle atmosphere levels is more sensitive to the option of cumulus scheme than other schemes (Yang et al. 2019), diversity cumulus schemes generate the different performance of simulated precipitation.

Particularly, the SAS scheme might be suitable for simulating the long-term climatological mean and seasonal propagation of rainfall over East Asia under current model settings. In addition, the performance of the simulated precipitation is also improved in KFMT after using a moisture-advection modulated trigger function, indicating the importance of the trigger function in cumulus scheme.

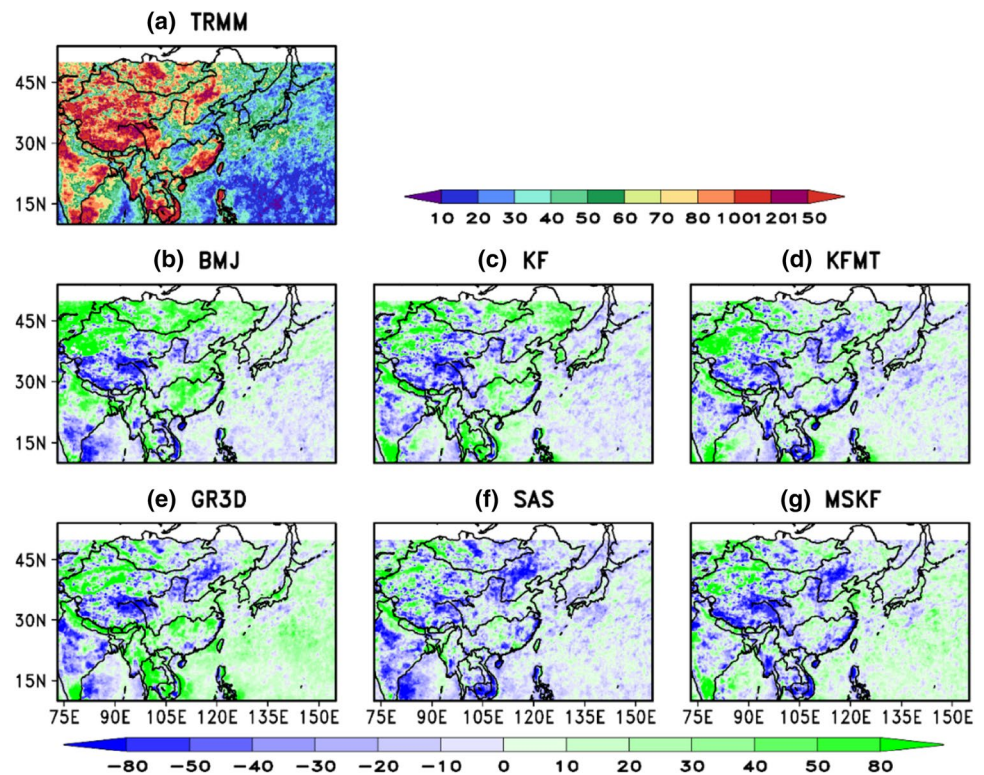## 3.2 Diurnal cycle of precipitation

3.2.1 The amplitude of the diurnal cycle of precipitation

As the amplitude of DCP always depends on the daily mean values, the normalized amplitude, which is defined as the ratio of the differences between the maximum and daily mean values to the daily mean values, is more appropriate for long-term evaluation. It is used in this study in order to weaken the influence of interannual variability. From the observations (Fig. 5a), a larger amplitude is found over land than the ocean. The maximum amplitudes are located along the coastal land regions of Southeast Asia and southern China, as well as in northwestern China and the Tibetan Plateau. Generally, WRF produces convincing spatial patterns and captures the locations of the maximum, regardless of the selected CPs (Fig. 5b–g). However, the simulated amplitudes are underestimated over the Tibetan Plateau, Yellow River Basin and Indian by all CPs. Notable discrepancies among the experiments exist over the other regions. For instance, the large positive biases over the northern parts of the

Fig. 4 Time-latitude cross section of pentad mean 850 hPa winds (vectors, unit: m s^{-1}) and vorticity (shading, unit: 10^{-5} s^{-1}) between 105°E and 123°E for reanalysis (**a**) and different convection schemes (**b–g**). The green contour lines indicate the zonal wind $u = 0$
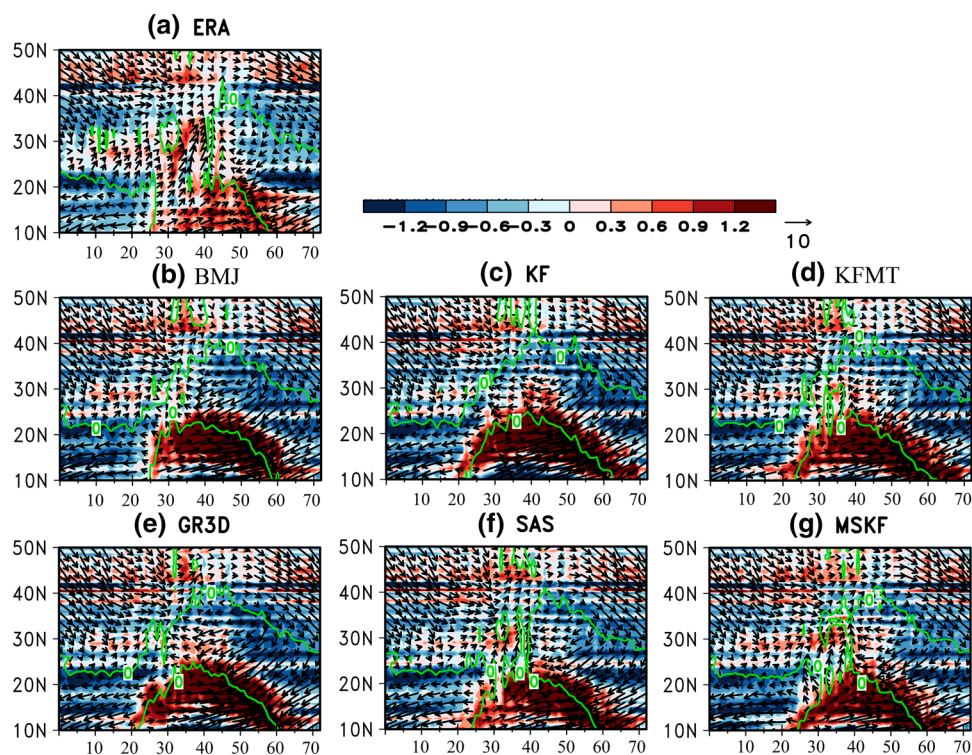
Fig. 5 The distribution of the normalized amplitude of diurnal precipitation in the observation (**a**) and the differences between the simulations and observation (**b**–**g**)

domain generated by BMJ and KF are effectively reduced by others. Meanwhile, GR3D and MSKF simulated higher amplitudes over the Western Pacific compared to the observations and other simulations.

3.2.2 The phase of the diurnal cycle of precipitation

The phase of diurnal variation is an important metric to examine the diurnal cycle. Figure 6 shows the diurnal peak time for summer PA over East Asia. Consistent with previous studies (Yu et al. 2007; Zhou et al. 2008), the rainfall maximum mainly occurs during the late morning to early afternoon over the ocean, and in the late afternoon over most of the land area. The early morning rainfall peak is found over the southern slope of the Tibetan Plateau and Sichuan Basin, which is associated with the effects of the mountain-forced gravity wave and regional-scale circulations (Barros and Lang 2003; Bao et al. 2011).

The land-sea contrast of peak times is captured by all simulations, and the inter-simulations differences are more apparent over the land than oceans. The simulated peak times over the oceans in each CP, with the exception of GR3D, are comparable to the features in the observation. GR3D generates a uniform peak time over the ocean areas south of 35°N, failing to reproduce the regional features. Moreover, the observed southward propagation over the Bay of Bengal is absent in the GR3D. Over the land areas, the simulated time of precipitation maximum mostly precedes

the observation, which is common in current climate simulations (Dai and Trenberth 2004). For instance, the afternoon peaks in the simulations mainly occur during 1400–1700 LST over eastern China, about 1–3 h earlier than the observation. Notable discrepancies between the observations and simulations exist over southern slope of the Tibetan Plateau, where the TRMM shows an early morning peak while most CPs present the maximum precipitation in the noon. It is worth noting that KFMT presents an encouraging improvement of simulated peak time over other CPs and thus bears a closer resemblance to the observation, with its peak time appearing approximately 5–6 h earlier for the southern slope of the Tibetan Plateau and 1–2 h later over eastern China than most of other CPs (Fig. 6 and supplementary Fig. 1). However, over the North China Plain, the KFMT shift the maximum precipitation from late afternoon to early morning.

The distributions of diurnal peak times for PF and PI (figures are not shown) are also analyzed to understand the model biases, because the various combinations of PF and PI can produce similar precipitation climatology in climate model (Dai 2006). The spatial patterns of PF peak time are similar to those of PA in both observation and simulations, indicating PF may play the predominant role in determining the phase of PA. All CPs show the limited skill in reproducing the spatial pattern of PI peaks. Relatively larger diversity exists for the simulated peak time over land than ocean. For instance, KFMT produces the delayed peak time over eastern

Fig. 6 Spatial distribution of the local time (LST) of maximum PA in diurnal variation from the observation (**a**) and model simulations with different convection schemes (**b**–**g**)
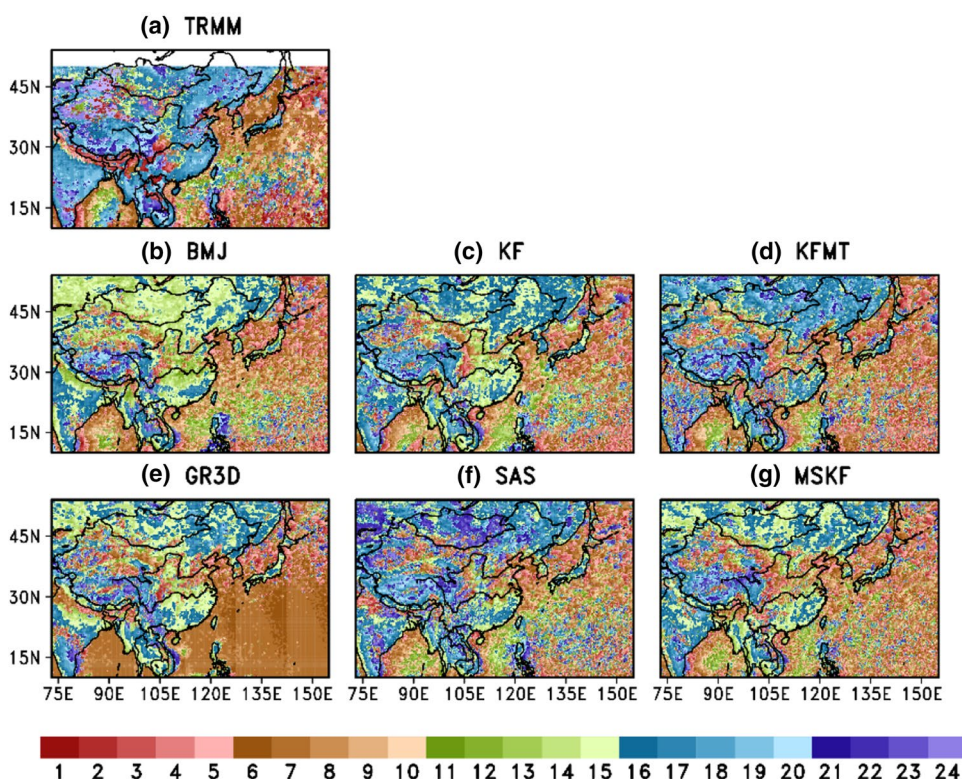
China while other CPs generate an earlier time compared to the observations.

As the summer precipitation over East Asia has large diurnal variations with considerable regional characters (Yu et al. 2007), we further divide East Asia into seven sub-regions based on distinct diurnal features, and evaluate the simulated diurnal cycle of precipitation against TRMM (Fig. 7). In observation, most of the sub-regions are dominated by an afternoon peak, which may be controlled by the high PF in the afternoon, while the nocturnal rainfall over the upper YRB (UYRB) may be contributed by intense PI during the night. Moreover, the PA over North China (NC) is featured by two peaks, with the largest at the afternoon and the other in the morning.

CPs strongly influence PA magnitudes, but little differences in the timing are found among the CPs expect KFMT. The performance of different CPs in simulating the diurnal cycle of PA depends on regions, and none of them performs better than others for all sub-regions. For example, KFMT outperforms other CPs in simulating the magnitudes and phases of PA over NEC, and displays advantages in simulating the timing but with large biases in magnitudes for other regions. The simulated PF is always higher and earlier than the observation over most sub-regions. Compared to KF, KFMT once again delays the afternoon peak of PF to about 1–2 h for all sub-regions, except NEC and India. Furthermore, KFMT could alleviate higher occurrence frequency, especially from 1300LST to 1500LST, when large

differences exist in PA between two simulations. These results demonstrate the importance of the trigger function for the rainfall diurnal cycle, especially for the peak time. The better performance in KFMT is attributed to the smaller temperature perturbation due to the modified trigger function based on moisture advection, as the reduced temperature perturbation influences the frequency of convective initiation (Choi et al. 2015). This, therefore, improves the diurnal variation of PF and delays the afternoon peak in PA with a reduced precipitation rate. In addition, the simulated magnitude and timing of PI are sensitive to the choice of CP, and all experiments fail to capture the diurnal cycle of PI shown in the observation.

3.2.3 Convective versus stratiform precipitation

To better understand the diversity among the CPs, the convective and stratiform precipitation are analyzed separately (Fig. 8). Strong and evident similarities between the peak times of convective precipitation and total rainfall suggest the dominating role of convective precipitation in determining the timing of diurnal rainfall cycle. Meanwhile, for the stratiform precipitation, all schemes simulate peak time in the early morning over most areas of the domain and at late night over the Tibetan Plateau, and the contract between the land and ocean is not as obvious as that for convective precipitation. Note that with the modified trigger function over the KF scheme, KFMT not only delays the peak time
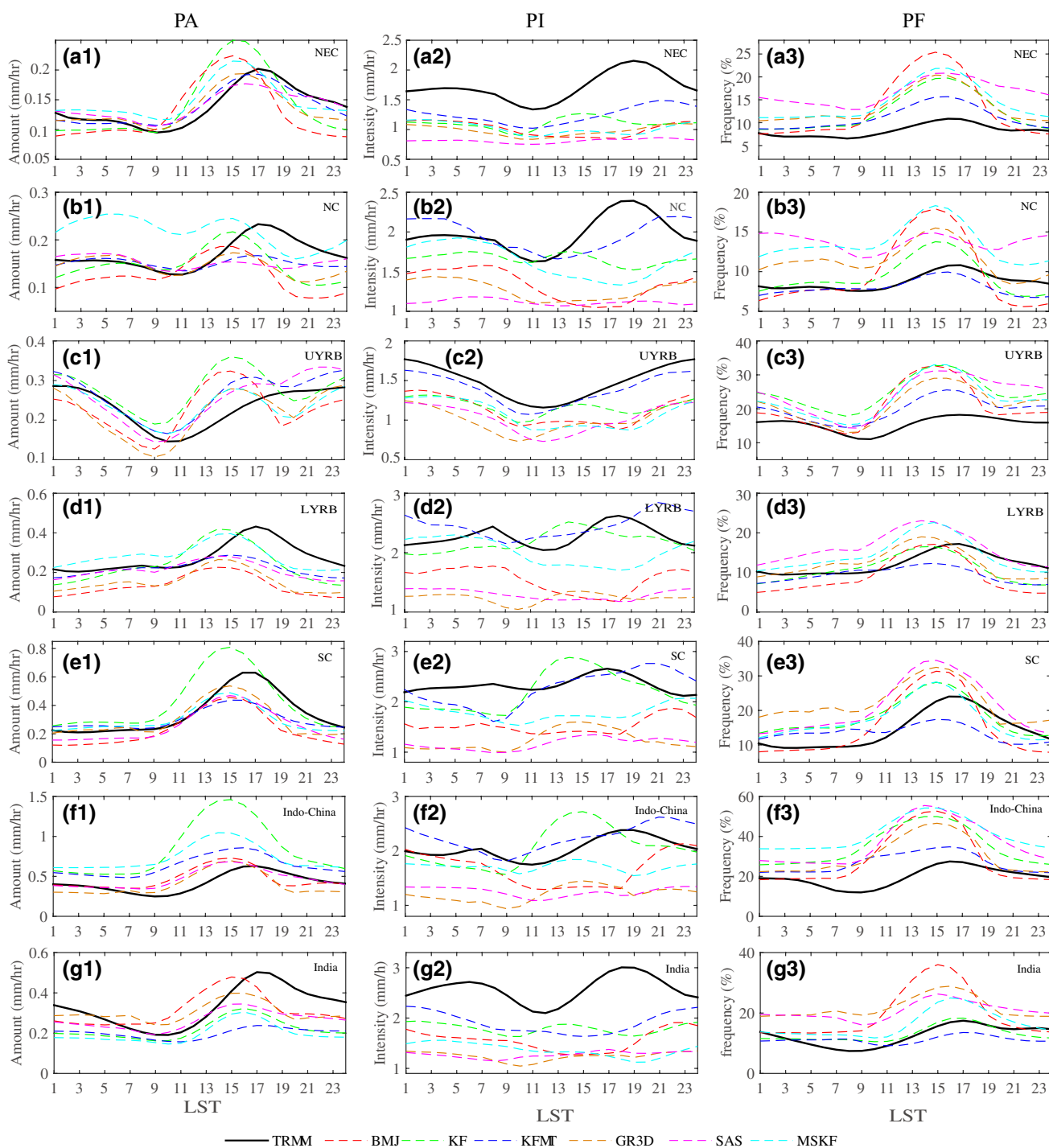
Fig. 7 Diurnal variations of PA, PI, and PF over the seven sub-regions in observation and the six convection schemes

of the convective precipitation over some of the land areas, such as NEC and lower YRB (LYRB), but also shifts the maximum stratiform precipitation from early morning to late afternoon over northern parts of the domain. These results contrast with an earlier study which suggests that the better performance in simulating the diurnal cycle of precipitation by KFMT over South Africa is due to the larger contribution

of stratiform precipitation rather than a delayed initiation of simulated convection (Pohl et al. 2014).

In contrast to the total precipitation, the diurnal cycle of convective precipitation shows little regional diversity, with the largest amount occurring at around 15-16LST and minimum late at night (Fig. 9). Although the patterns of convective precipitation appear to be physics-independent,

Fig. 8 Comparisons of the local time (LST) for maximum stratiform and convective precipitation in simulated diurnal variation among the six experiments
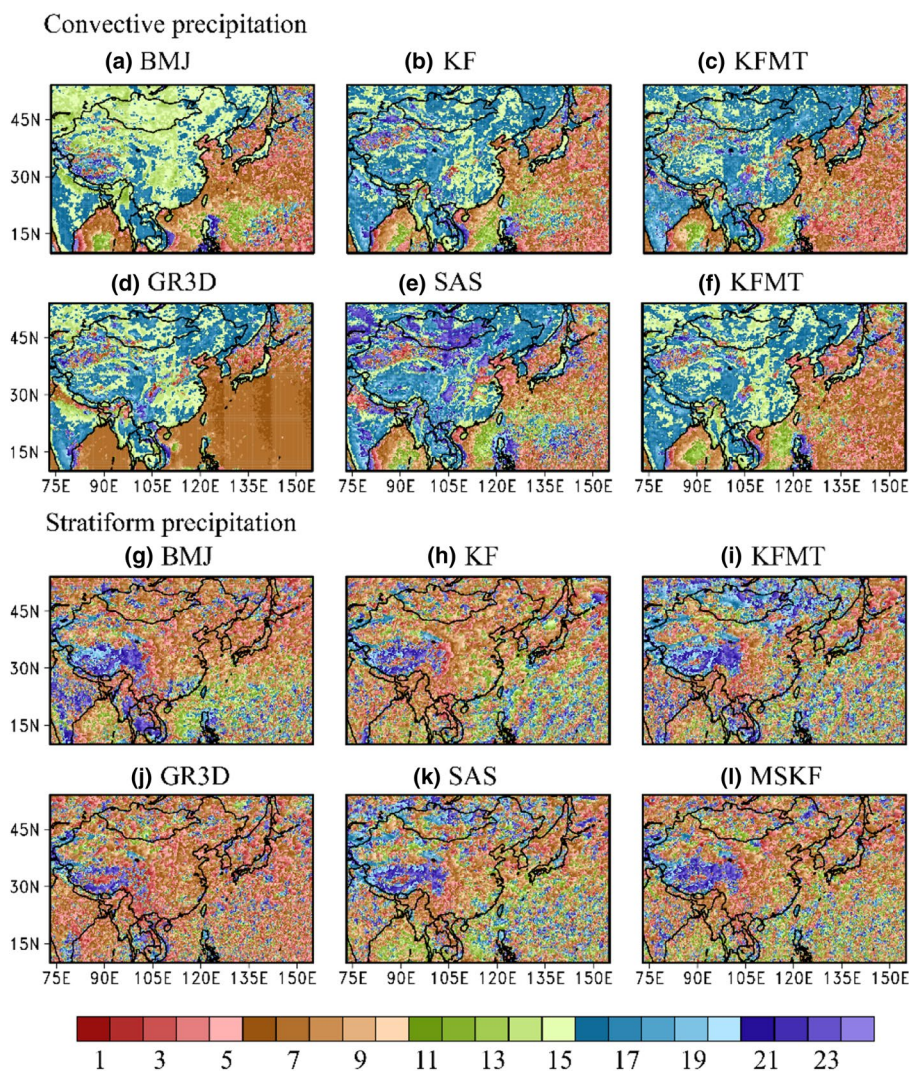
the magnitudes differ greatly from one experiment to another. For example, the values generated by KF are about 1.5 to 2 times higher than those in KFMT experiment. Note that BMJ produces the least convective rainfall from late night to early morning, and even no convective rainfall over some regions. This phenomenon is also found over South Africa (Pohl et al. 2014) and requires further analysis. As the diurnal rainfall primarily follows the convective precipitation over most of the sub-regions, the unrealistic early afternoon peaks in total rainfall may be caused by the incorrect onset of convection. For the stratiform precipitation, the valleys always appear at noon and the peaks occur late at night over UYRB and in the morning over other regions. The timing and magnitude of stratiform precipitation are sensitive to the choice of the CP. For instance, GR3D generates less stratiform precipitation and advances the peak time by 1–2 h than others.

These disagreements illustrate that the CPs could indirectly affect stratiform precipitation through modifying atmospheric instability and the amount of precipitation water left in the air column (Pohl et al. 2014).

Compared to KF, KFMT reduces the amount of convective precipitation and postpones the maximum by about 1–2 h over some sub-regions, such as NC, UYRB, LYRB, and India. It increases the amount of stratiform rainfall and generates an extra evening peak (around 1900-2000LST) over NEC and NC in additional to the morning peak. After modifying the trigger function in KF, the percentages of convective rainfall to total amount in KFMT are effectively reduced, which is similar in shape to the observations (supplementary Fig. 2f). These results confirm that the description of the onset criterion for atmospheric convection in the model strongly impacts both the climatic and diurnal cycles of precipitation (Dai and Trenberth 2004).
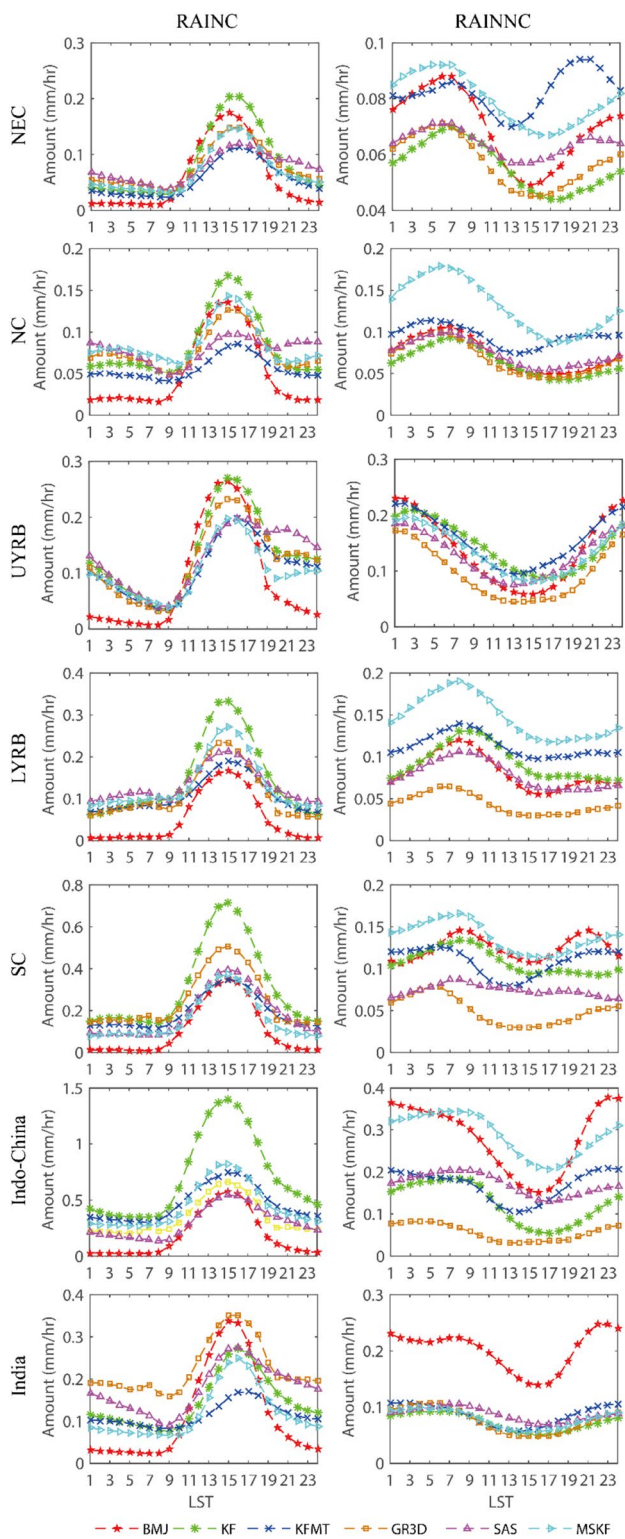
Fig. 9 Diurnal variations of convective (RAINC, left column) and stratiform (RAINNC, right column) precipitation over the seven sub-regions

3.2.4 Propagating feature of DCP along the Yangtze River Basin

One interesting aspect in DCP over East Asia is the distinct eastward propagation of the diurnal phase along YRB. Figure 10 shows the time-longitude diagrams of observed and simulated rainfall over the YRB (averaged between 26 and 34°N) to assess the performance of CPs in simulating the propagating feature of DCP. The propagating rainfall system develops in the afternoon over the Tibetan Plateau, and then moves eastward from the foothill of Tibetan Plateau at night until it reaches the middle of YRB next morning. This phase-shift is less evident over the area east of 110°E, where the peaking precipitation occurs around 16 LST.

All simulations could replicate the features of the two rainfall systems and show that the propagating rainfall system to the west of 110°E is mainly controlled by stratiform precipitation, and the rainfall system over LYRB is associated with local convection. Compared to observation, the propagating rainfall system is comparatively weak in BMJ and GR3D with shorter distance and lifetime indicating the poor stratiform precipitation simulation. A spurious afternoon rainfall (around 1500 LST) over the UYRB is generated by the KF scheme owing to the overestimation of the convective precipitation, although it could successfully capture the propagating rainfall system. Among all CP options, KFMT and SAS perform well in depicting the eastward propagation in terms of both amplitude and time. For the areas east of 110°E, all CPs capture the afternoon rainfall peak, with the advanced peak time and weakened magnitude. The KF scheme shows a clear advantage over others in depicting the magnitude of rainfall and KFMT once again corrects the early-shifted phase.

3.2.5 Possible mechanisms for diverse simulation among CPs

To investigate the possible mechanisms leading to the different diurnal rainfall among the simulations, we compare model performance in reproducing the diurnal cycle of large-scale circulations by showing the deviations of the low-level (850 hPa) vertical motion and vertically integrated moisture flux (Fig. 11). We also present the corresponding specific humidity and vertical motions, as well as the perturbation vertical circulations averaged between 26 and 34°N (Fig. 12). For convenience, we use Beijing Standard Time (BJT) in this section.

Consistent with previous studies (Li et al. 2018; Yuan et al. 2012), the moisture flux anomalies experience a clockwise rotation toward the TP, bringing a moist air mass to the UYRB and resulting in a positive deviation of specific humidity in the early evening (2000 BJT). A strengthened upward motion is found over the eastern periphery of the

Fig. 10 Time-longitude diagrams of observed (**a**) and simulated rainfall with different convection schemes (**b**–**g**) over the Yangtze River Basin (averaged between 26°N and 34°N) during summer. The simulated convective and stratiform precipitation above 0.25 mm h^{-1} are denoted in black and gray lines at an interval of 0.05 mm h^{-1}
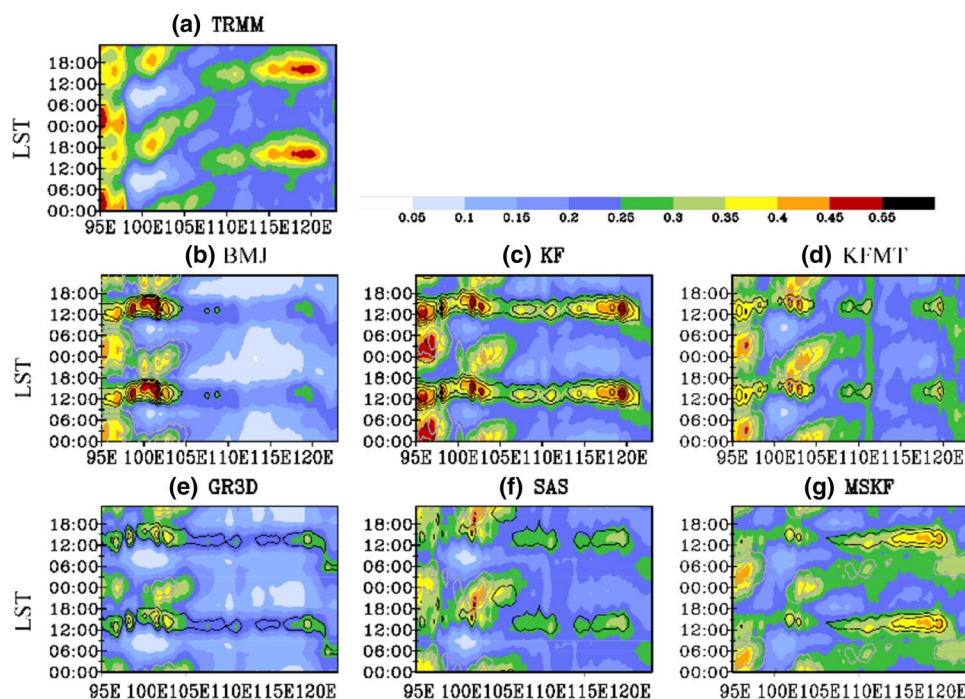
TP, while a descending motion dominates over most of East China at that time. Such a circulation pattern is favorable for the nocturnal rainfall over the eastern slope of the TP and a suppressed phase of the precipitation over east China. At 0200 BJT, the anomalous southwest moisture fluxes prevail over East China and even reach up to North China. The acceleration of the southwesterly flow not only leads to the increase of specific humidity but also causes the low-level convergence over the middle YRB, which facilitate midnight rainfall there. The comparatively large rainfall over North China at midnight can be partly explained by the strengthened southwest moisture flux and ascending motion in this area. As is revealed in Figs. 11 and 12, the anomalous atmospheric circulations at 0800 BJT are contrary to those at 2000 BJT. The UYRB is occupied by the sinking branch and dry environment, which are in accordance with the minimum phase of precipitation at this hour. Meanwhile, the southwesterly flow and northwesterly flow converge over the LYRB, resulting in the upward motion at the lower-mid troposphere. In the afternoon (1400 BJT), the northerly flow dominates East China (Fig. 11a2) with negative specific humidity deviations over the TP and positive deviations over the lower YRB (Fig. 12a2). Additionally, the ascending flow is found over most of East China, which may be associated with the afternoon development of convection systems and strong convection rainfall. In addition, the ascending flow moves eastward accompanied by a large center of specific humidity which contributes to the eastward propagation of the rainfall system.

The six experiments present comparable diurnal variations of circulations to the reanalysis in terms of wind directions, although they have amplitudes biases. Compared to the observations, the simulated water vapor transport shows a larger diurnal variation, which is associated with the biases in the simulated rainfall diurnal amplitude. The feature that the water vapor comes from northwesterly and southwesterly directions and converges over the LYRB in the morning is absent in the BMJ and GR3D simulations, which results in weaker upward motions (Fig. 12b1 and e1) and dry biases. Moreover, the biases in water vapor transport are more evident during the daytime (0800 and 1400) over the western North Pacific.

As the vertically integrated moisture flux is mainly controlled by the lower atmosphere (Zhou and Yu 2005), the biases in the simulated low-level water vapor transport are examined (Fig. 13). There exists a systematic bias in all simulations for the whole day. A significant anomalous low-level cyclone is found over the western North Pacific, which results in a strong westerly flow over the areas around 20°N. Those westerly flow biases, accompanied by greater vertical velocity, lead to the wet biases in this area. Weaker southwesterly winds over eastern China are found in all simulations, and MSKF significantly reduces the bias and produces the largest regional rainfall. The biases in low-level water vapor transport are unfavorable for the extensive rainfall over eastern China, suggesting the wet biases over the LYRB in the KF and MSKF experiments in the afternoon may be contributed to the convection activity.

Figure 14 examines the vertical profile of afternoon moisture static energy (MSE) over the LYRB as an example to investigate the environment conditions for convection development. The definition of MSE is:

$$MSE = c_p T + L_v q + gz$$

where T is the air temperature, q represents the specific humidity, and z means the geopotential height. c_p, L_v, and g refer to the specific heat of air, the latent heat of water vaporization, and the gravitational acceleration, respectively. As the unstable atmosphere has a decreasing MSE with altitude, MSE has been widely used in analyzing the instability associated with precipitation (Pu and Cook 2012; Neupane and Cook 2013).

The MSE anomaly at 1400 BJT over the LYRB is mainly confined below 700 hPa, and the development of MSE gradients below that level indicates an enhanced instability in the lower-troposphere, which results in an ascending motion and rainfall. All simulations show a reasonable MSE profile, indicating that the simulated environmental conditions do not deviate too much from the observed states. Compared to the ERA-IN, the simulated MSE anomaly profile is more unstable below 700 hPa, particularly in the KF simulation. Thus, the wet biases in the afternoon over the LYRB in the KF simulation may be explained by the largest positive perturbations in the lower level atmosphere.

The diurnal variations in the geopotential are negligible (Neupane and Cook 2013). Therefore, we separate the temperature and moisture contributions to the MSE (Fig. 14b and c). The thermal contribution dominates the anomalous MSE near the surface and the moisture contribution stabilizes at the lower troposphere (around 850–700 hPa) in both reanalysis and simulations. However, the positive anomalies in CpT term between 850–700 hPa in the reanalysis are absent in all simulations, suggesting that models underestimate thermal contributions in lower troposphere. The enhanced vertical transport of humidity is found in all simulations, especially in the KF, which is in accord with the excessive precipitation in this experiment.

4 Summary and discussion

In this study, we present the sensitivity of the summer mean and diurnal precipitation to the cumulus scheme over COR-DEX-EA-II domain by using WRF, with focus on eastern China. The different performance in simulating the precipitation characteristics among CPs is also examined by comparing the large-scale circulation variations.

All CPs could reasonably capture the distributions of summer mean PA and the broad migration of the rain belt, although they have large biases, which depend on the choice of CP. All simulations overestimate the oceanic precipitation, especially over the ocean south of 30°N. The biases

of the seasonal march of rainfall in BMJ, KF, and GR3D are related to the deficiency in low-level winds and weakened northward propagation of the cyclonic vorticity. Other CPs improve the simulation of the southwesterly flow and cyclonic vorticity over the subtropics, and therefore their results resemble the observations better. Comparatively, the SAS scheme might be the most suitable for simulating the long-term climatological mean and seasonal propagation of rainfall over East Asia, because of higher CORR and lower RMSE under current model settings. Moreover, the performance in depicting climatological state is better in KFMT after modifying the trigger function, indicating the importance of the trigger function in the cumulus scheme.

Regarding to the diurnal variation, the differences in precipitation diurnal phases are more apparent over land than ocean among the simulations. Consistent with the observations, the simulated peak time over the ocean appears in the late morning to early afternoon. However, the simulated precipitation maximum mostly precedes the observations by about 1–3 h, which is a common problem in model (Dai et al. 1999; Yuan et al. 2013) and may be related to deficiencies in simulating PF. All the CPs show limited skills in reproducing the PI in terms of magnitude and phase. KFMT bears a closer resemblance to the observations in terms of the diurnal cycle phase, such as the nocturnal precipitation over the southern slope of the Tibetan Plateau and Sichuan Basin, and the delayed peak time over eastern China. Nevertheless, it still shows disadvantage in the magnitudes over some sub-regions. The performance of different CPs in simulating the diurnal cycle of PA depend on regions, and none of them performs better than the others for all the sub-regions. The separated analysis of total precipitation into convective and stratiform precipitation indicates that CPs not only affect the magnitude of convective precipitation, but also the timing and magnitude of stratiform precipitation.

We also inspect the diurnal circulation features and local atmospheric stability in this study. All the simulations reproduce the diurnal clockwise rotation of the vertically integrated moisture flux shown in ERA-IN with a larger diurnal variation, which is consistent with the nocturnal eastward propagating rainfall system over the YRB. However, BMJ and GR3D fail to simulate the feature that the southwesterly merges with the northwesterly over the LYRB in the morning (about 0800 BST), which is shown in the reanalysis data and other simulations. This leads to weaker upward motions and dry biases at that time in the two simulations. Further analysis shows that the excessive afternoon rainfall over the LYRB in KF and MSKF can be explained by the largest positive perturbation in the lower level atmosphere, as the simulated MSE profile becomes more unstable below 700 hPa, particularly in the KF experiment. All the CPs underestimate the thermal contributions to the anomalous MSE in the lower troposphere, while they overestimate the
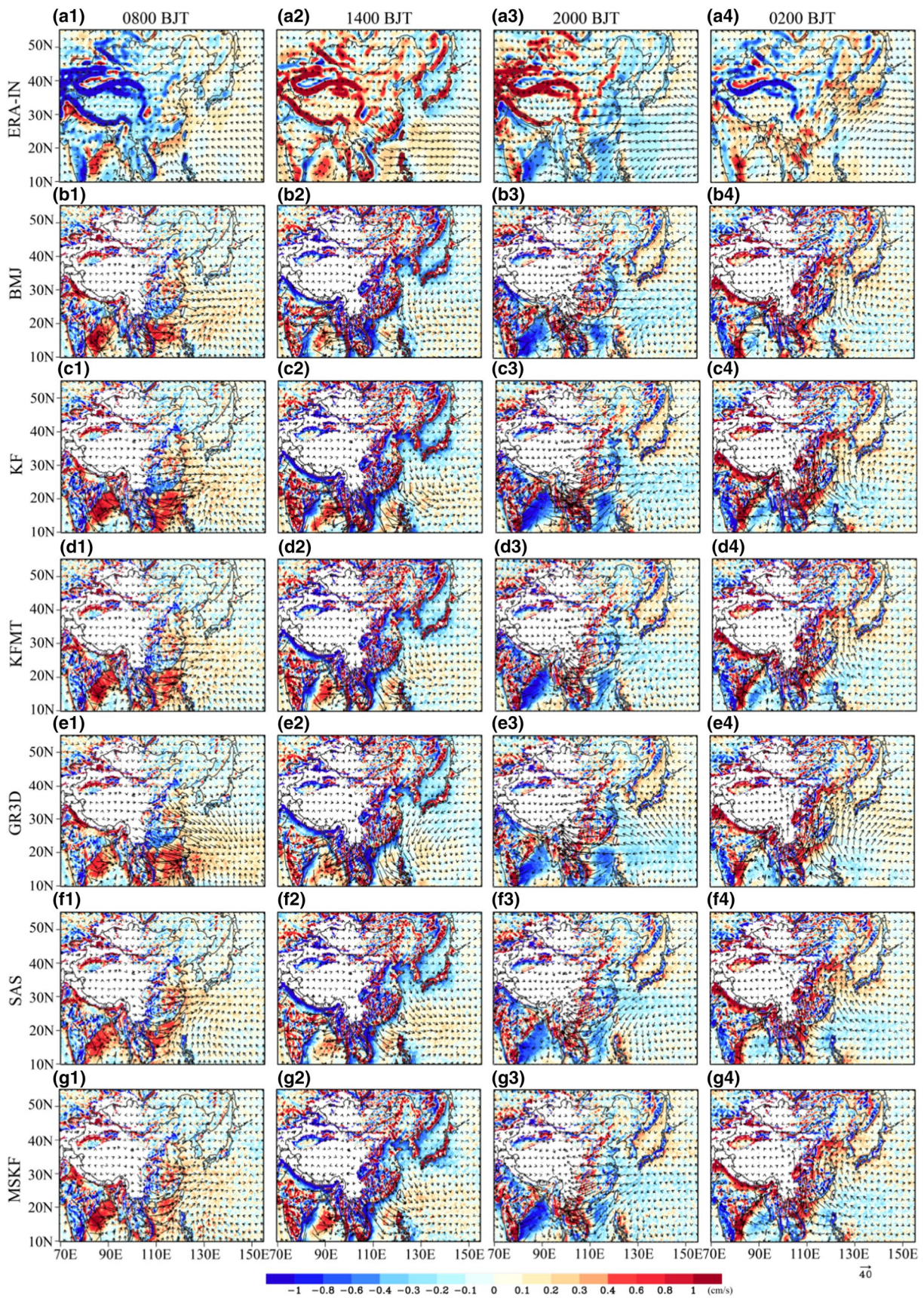
◄**Fig. 11** The deviations of vertically-integrated moisture flux (vectors, unit: kg m^{-1} s^{-1}) and vertical motion (shading, unit: cm s^{-1}) at 850 hPa at 0800 Beijing Standard Time (BJT), 1400BJT, 2000BJT, and 0200BJT in ERA-IN (**a1**–**a4**) and simulations (**b1**–**g4**). The pressures higher than 850 hPa are masked out in the simulations

moisture contributions. The enhanced vertical transport of humidity in KF is in accord with the excessive afternoon precipitation in this experiment.

Based on different principles, each CP has its own representation of cumulus convection, and the primary components in CP, including the trigger function, closure assumption, and the mass flux formulation, have a significant influence on the simulation. For example, the effect of trigger function on the simulated precipitation during the EASM period can be drawn through comparing the simulations between KF and KFMT. Compared to the results from KF, KFMT could reasonably eliminate convective instability under weak synoptic forcing, thus leading to a more comparable distribution of convective rain ratio and better simulation of diurnal cycle phase (Ma and Tan 2009; Choi et al. 2015). Different cumulus closures lead to diversity in distributions of cloud base mass flux and atmospheric instability, as well as large-scale updrafts, ultimately affecting the simulated precipitation (Qiao and Liang 2016). The KF scheme based on the total instability removal closure assumption generally yield large wet bias along the coast oceans (Liang et al. 2004b). Different from other CPs which are mass flux schemes, BMJ is an adjustment type scheme, and it forces the model vertical profile at each point toward a reference profile (Arakawa 2004). Such a fixed reference humidity profile in BMJ leads to an excessive precipitation over most of Southeast Asia, which could be alleviated when the humidity reference profile moves towards more moisture (Fonseca et al. 2015). As CP is extremely complex and contains many other variable parameters, further analysis needs to systematically identify those components in the CP.

This study evaluates the performance of different cumulus parameterization schemes in reproducing seasonal and diurnal variation of rainfall over CORDEX-EA-II, which provides useful information to understand the physical biases and main process of rainfall in the model. However, there is still a number of limitations that should be taken into account.

Firstly, the model still has large deficiencies in simulating precipitation frequency and intensity, as well as the low-latitude oceanic precipitation, which are attributed to the incomplete description or poor representation precipitation processes in the model. Convections can be too easily triggered in the model, and the simulation of Asian summer monsoon precipitation would be improved if the convective suppression criteria are employed in the cumulus (Emori et al. 2001; Zou and Zhou 2013). It should be noted that the anomalous convective activities in the western North Pacific can affect the precipitation over LYRB due to the Rossby wave (Sun et al., 2016b, 2019). The excessive oceanic precipitation over low-latitude areas is also associated with the incorrect simulation of the western Pacific subtropical high, which may be contributed by the non-consideration of the air-sea interaction and unemployment of spectral nudging in all experiments. The implementation of coupled air-sea interaction or spectral nudging in the RCM could significantly improve the regional climate simulation of the EASM, especially for the simulation of western North Pacific summer monsoon (Fonseca et al. 2015; Kim and Hong 2010; Zou and Zhou 2014).

Secondly, the simulated precipitation is closely related to domain size (Dash et al. 2015) and model resolution (Dirmeyer et al. 2012; Jin et al. 2016), as well as other physics parameterizations, such as the planetary boundary layer (PBL) scheme (Sun et al. 2016a; Yang et al. 2018) and land surface scheme (Pei et al. 2014; Kang et al. 2015). Moreover, the sensitivity of the diurnal peak time of rainfall to the convective parameterization schemes can be modulated by the resolution (Jin et al. 2016) and PBL vertical resolution (Yang et al. 2018). Therefore, how convective parameterization schemes interact with other schemes warrants further investigations.

Thirdly, observation reveals that the features of the East Asian summer monsoon vary hugely during different rainy stages in terms of spatial distribution as well as the propagation speed and the eastward extent of the diurnal peak (Bao et al. 2011; Xu 2013). Further analysis results indicate that the skills in simulating the distribution of monthly mean precipitation are different during the summer monsoon for all CPs, with a better performance in May and August (supplementary Fig. 3). In particularly, SAS generally present better consistency with the observations than other CPs in all the months under current model settings, which may be related to its comparable performance in capture the circulation feature during the monsoon. Besides that, the sensitivity of the diurnal cycle to cumulus parameterization schemes is different between the pre-monsoon and monsoon seasons (He et al. 2015). Hence, the study period can be divided into different rainy periods in the future to better identify how the precipitation will respond to the convective parameters during those periods.

Finally, the assumptions in convective parameterization might not be accurate enough for the CORDEX-EA-II domain. To avoid this problem, a convection-permitting model, which explicitly resolves rather than parameterizes convection and shows improvements in precipitation frequency and intensity (Dai et al. 2017) as well as the diurnal variation (Ban et al. 2014; Li et al. 2018), can be used. Nevertheless, those improvements do not guarantee a better simulation of mean precipitation (Cash et al. 2015) and the
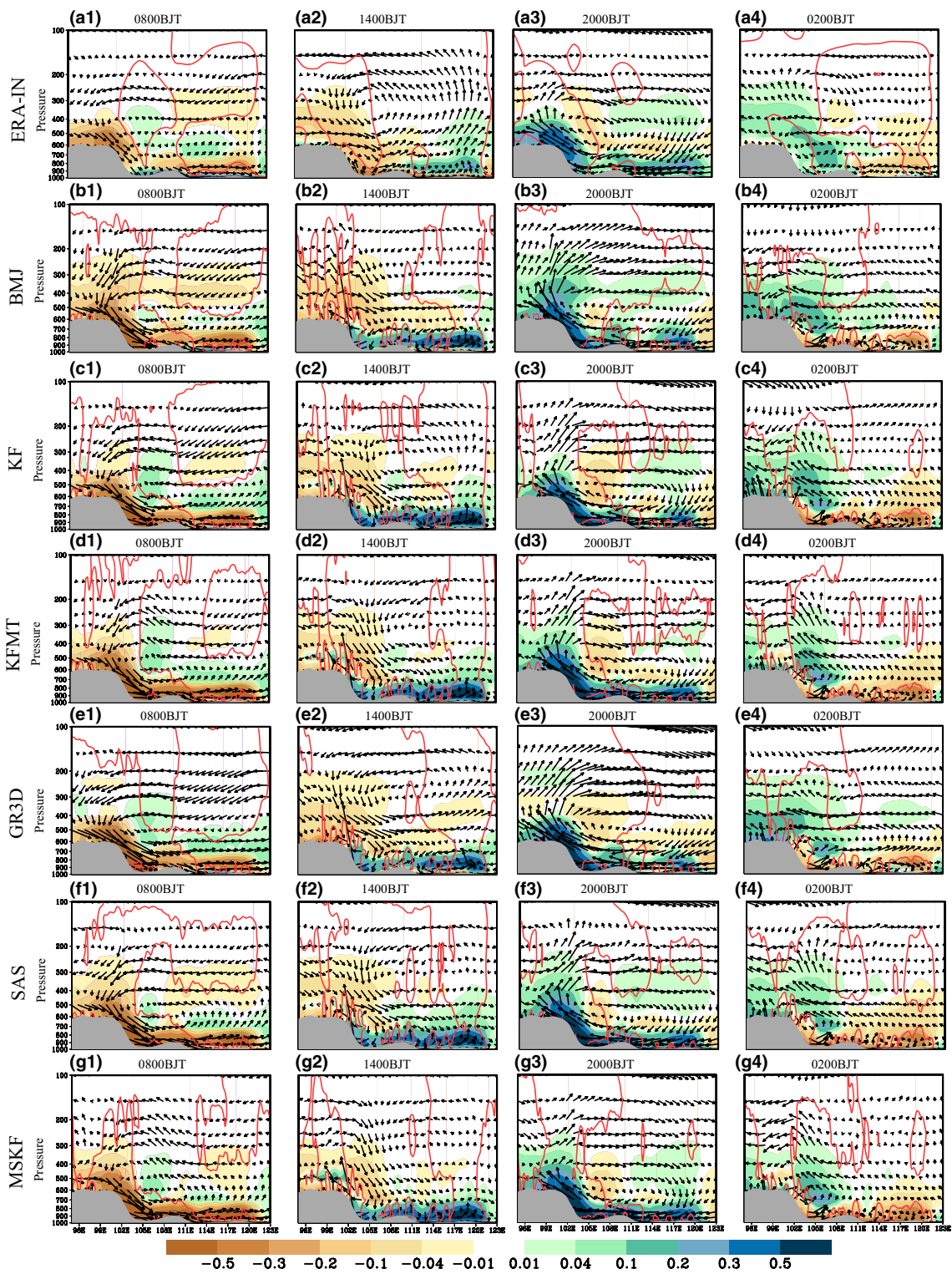
Fig. 12 East-west cross sections of the longitude-vertical circulation anomalies (vectors, the unit of zonal wind is m s⁻¹ while for vertical velocity is 2*10⁻²m s⁻¹) and specific humidity anomalies (shading, unit: q kg⁻¹), as well as vertical motions anomalies at 0 m s⁻¹ (red line, unit: cm s⁻¹) averaged between 26 and 34°N at 0800BJT, 1400BJT, 2000BJT, and 0200BJT in ERA-IN (**a1**–**a4**) and simulations (**b1**–**g4**)
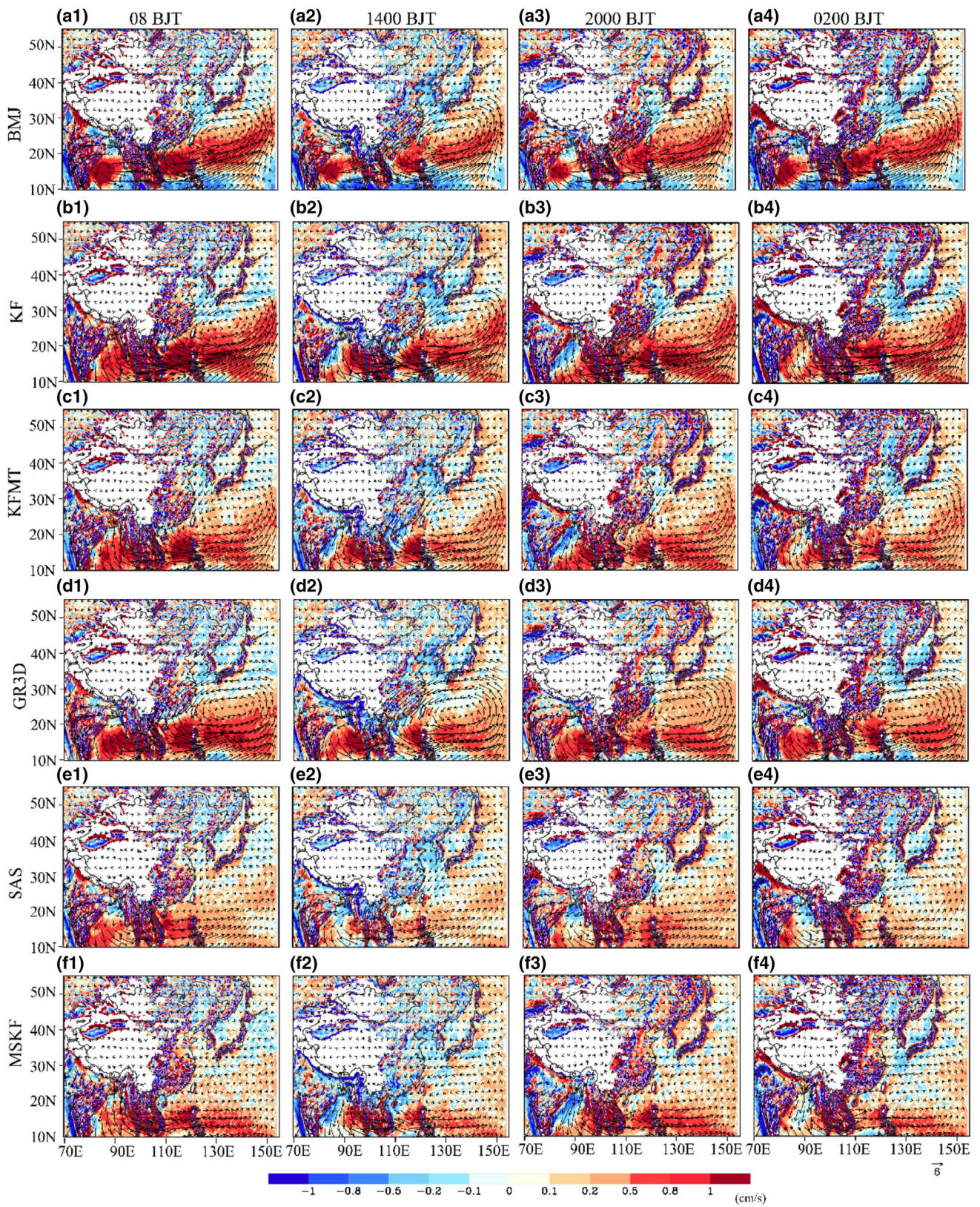
Fig. 13 The biases in the simulated water vapor transport (vector, unit: g cm^{-1} hPa^{-1} s^{-1}) and vertical velocity (shading, unit: cm s^{-1}) at 850 hPa

Fig. 14 Profiles of total MSE (**a**), temperature term (**b**), and moisture component (**c**) anomalies (unit: 10^{-3} m^2 s^{-2}) averaged over the LYRB at 1400 BJT in the ERA-IN and simulations
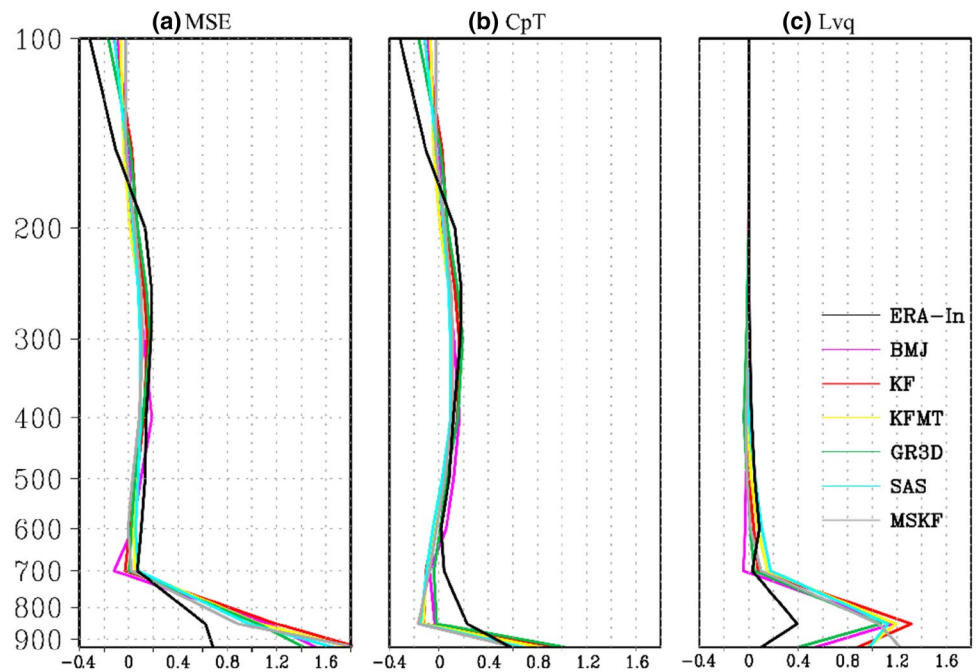
long-term simulation over large domain is still limited by the current computational capability. The question of how the physical processes associated with convection should be partitioned between the parameterized and resolved parts requires deeper understanding.

References

Arakawa A (2004) The cumulus parameterization problem: past, present, and future. J Clim 17:2493–2525
Ban N, Schmidli J, Schär C (2014) Evaluation of the convection-resolving regional climate modeling approach in decade-long simulations. J Geophys Res Atmos 119:7889–7907
Bao X, Zhang F, Sun J (2011) Diurnal variations of warm-season precipitation east of the Tibetan Plateau over China. Mon Weather Rev 139:2790–2810. https://doi.org/10.1175/mwr-d-11-00006.1
Barros AP, Lang TJ (2003) Monitoring the monsoon in the Himalayas: observations in Central Nepal, June 2001. Mon

Weather Rev 131:1408–1427. https://doi.org/10.1175/1520-0493(2003)131%3c1408:mtmith%3e2.0.co;2
Bechtold P, Chaboureau J-P, Beljaars A, Betts AK, Köhler M, Miller M, Redelsperger J-L (2004) The simulation of the diurnal cycle of convective precipitation over land in a global model. Q J R Meteorol Soc 130:3119–3137. https://doi.org/10.1256/qj.03.103
Bechtold P, Semane N, Lopez P, Chaboureau J-P, Beljaars A, Bormann N (2014) Representing equilibrium and nonequilibrium convection in large-scale models. J Atmos Sci 71:734–753. https://doi.org/10.1175/jas-d-13-0163.1
Betts AK, Miller MJ (1986) A new convective adjustment scheme. Part II: Single column tests using GATE wave, BOMEX, ATEX and arctic air-mass data sets. Q J R Meteorol Soc 112:693–709. https://doi.org/10.1002/qj.49711247308
Cash BA et al (2015) Regional structure of the Indian summer monsoon in observations, reanalysis, and simulation. J Clim 28:1824–1841
Chen F, Dudhia J (2001) Coupling an advanced land surface-hydrology model with the Penn State–NCAR MM5 modeling system. Part I: Model implementation and sensitivity. Mon Weather Rev 129:569–585. https://doi.org/10.1175/1520-0493(2001)129%3c0569:caalsh%3e2.0.co;2
Chen H, Yu R, Li J, Yuan W, Zhou T (2010) Why nocturnal long-duration rainfall presents an eastward-delayed diurnal phase of rainfall down the Yangtze River valley. J Clim 23:905–917. https://doi.org/10.1175/2009jcli3187.1
Chen S, Yan Y, Liu G, Fang D, Wu Z, He J, Tang J (2018) Spatiotemporal characteristics of precipitation diurnal variations in Chongqing with complex terrain. Theoret Appl Climatol. https://doi.org/10.1007/s00704-018-2662-7
Choi I-J, Jin EK, Han J-Y, Kim S-Y, Kwon Y (2015) Sensitivity of diurnal variation in simulated precipitation during East Asian summer monsoon to cumulus parameterization schemes. J Geophys Res Atmos 120:11,971–911,987 https://doi.org/10.1002/2015jd023810
Collins WD, Rasch PJ, Boville BA, Hack JJ, McCaa JR, Williamson DL, Kiehl JT, Briegleb B (2004), Description of the NCAR Community Atmosphere Model (CAM 3.0), Tech. Rep. NCAR TN-464+STR, National Center for Atmospheric Research

Dai A (2006) Precipitation characteristics in eighteen coupled climate models. J Clim 19:4605–4630. https://doi.org/10.1175/jcli3884.1

Dai A, Trenberth KE (2004) The diurnal cycle and its depiction in the community climate system model. J Clim 17:930–951. https://doi.org/10.1175/1520-0442(2004)017%3c0930:tdcaid%3e2.0.co;2

Dai A, Giorgi F, Trenberth KE (1999) Observed and model-simulated diurnal cycles of precipitation over the contiguous United States. J Geophys Res Atmos 104:6377–6402

Dai A, Rasmussen RM, Liu C, Ikeda K, Prein AF (2017) A new mechanism for warm-season precipitation response to global warming based on convection-permitting simulations. Clim Dyn. https://doi.org/10.1007/s00382-017-3787-6

Dash SK, Pattnayak KC, Panda SK, Vaddi D, Mamgain A (2015) Impact of domain size on the simulation of Indian summer monsoon in RegCM4 using mixed convection scheme and driven by HadGEM2. Clim Dyn 44:2331. https://doi.org/10.1007/s00382-015-2495-3

Dee DP, Uppala SM, Simmons AJ, Berrisford P, Poli P, Kobayashi S, Andrae U, Balmaseda MA, Balsamo G, Bauer P, Bechtold P, Beljaars ACM, van de Berg L, Bidlot J, Bormann N, Delsol C, Dragani R, Fuentes M, Geer AJ, Haimberger L, Healy SB, Hersbach H, Hólm EV, Isaksen L, Kållberg P, Köhler M, Matricardi M, McNally AP, Monge-Sanz BM, Morcrette J-J, Park B-K, Peubey C, de Rosnay P, Tavolato C, Thépaut J-N, Vitart F (2011) The ERA-Interim reanalysis: configuration and performance of the data assimilation system. Q J R Meteorol Soc 137(656):553–597

Ding Y, Chan JCL (2005) The East Asian summer monsoon: an overview. Meteorol Atmos Phys 89:117–142

Dirmeyer PA et al (2012) Simulating the diurnal cycle of rainfall in global climate models: resolution versus parameterization. Clim Dyn 39:399–418

Emori S, Nozawa T, Numaguti A, Uno I (2001) Importance of cumulus parameterization for precipitation simulation over East Asia in June. J Meteorol Soc Jpn 79:939–947

Folkins I, Mitovski T, Pierce JR (2014) A simple way to improve the diurnal cycle in convective rainfall over land in climate models. J Geophys Res Atmos 119:2113–2130

Fonseca RM, Zhang T, Yong KT (2015) Improved simulation of precipitation in the tropics using a modified BMJ scheme in the WRF model. Geosci. Model Dev 8:2915–2928. https://doi.org/10.5194/gmd-8-2915-2015

Fu C et al (2005) Regional climate model intercomparison project for Asia. Bull Am Meteorol Soc 86:257–266. https://doi.org/10.1175/bams-86-2-257

Gao X, Shi Y, Zhang D, Wu J, Giorgi F, Ji Z, Wang Y (2012) Uncertainties of monsoon precipitation projection over China: Results from two high resolution RCM simulations. Clim Res 52:213–226

Gao Y, Leung LR, Zhao C, Hagos S (2017) Sensitivity of U.S. summer precipitation to model resolution and convective parameterizations across gray zone resolutions: sensitivity across gray zone resolutions. J Geophys Res Atmos 122:2714–2733

Gianotti RL, Zhang D, Eltahir EAB (2012) Assessment of the regional climate model version 3 over the maritime continent using different cumulus parameterization and land surface schemes. J Clim 25:638–656. https://doi.org/10.1175/jcli-d-11-00025.1

Giorgi F, Lionello P (2007) Climate change projections for the Mediterranean region. Glob Planet Change 63:90–104

Giorgi F, Jones C, Asrar GR (2009) Addressing climate information needs at the regional level: the CORDEX framework. Bull World Meteorol Organ 58(3):175–183

Grell GA, Dévényi D (2002) A generalized approach to parameterizing convection combining ensemble and data assimilation techniques. Geophys Res Lett 29:38-31–38-34 doi:https://doi.org/10.1029/2002gl015311

Han J, Pan H-L (2011) Revision of convection and vertical diffusion schemes in the NCEP global forecast system. Weather Forecast 26:520–533. https://doi.org/10.1175/waf-d-10-05038.1

He H, Zhang F (2010) Diurnal variations of warm-season precipitation over Northern China. Mon Weather Rev 138:1017–1025. https://doi.org/10.1175/2010mwr3356.1

He X et al (2015) The diurnal cycle of precipitation in regional spectral model simulations over West Africa: sensitivities to resolution and cumulus schemes. Weather Forecast 30:424–445

Hong S-Y, Noh Y, Dudhia J (2006) A new vertical diffusion package with an explicit treatment of entrainment processes. Mon Weather Rev 134:2318–2341. https://doi.org/10.1175/mwr3199.1

Janjić ZI (1994) The step-mountain eta coordinate model: further developments of the convection, viscous sublayer, and turbulence closure schemes. Mon Weather Rev 122:927–945. https://doi.org/10.1175/1520-0493(1994)122%3c0927:tsmecm%3e2.0.co;2

Jin EK, Choi IJ, Kim SY, Han JY (2016) Impact of model resolution on the simulation of diurnal variations of precipitation over East Asia. J Geophys Res Atmos 121:1652–1670

Kain JS, Fritsch JM (1990) A one-dimensional entraining/detraining plume model and its application in convective parameterization. J Atmos Sci 47:2784–2802. https://doi.org/10.1175/1520-0469(1990)047%3c2784:aodepm%3e2.0.co;2

Kang HS, Hong SY (2008) Sensitivity of the simulated East Asian summer monsoon climatology to four convective parameterization schemes. J Geophys Res Atmos 113:D15119. https://doi.org/10.1029/2007JD009692

Kang S, Im ES, Ahn JB (2015) The impact of two land-surface schemes on the characteristics of summer precipitation over East Asia from the RegCM4 simulations. Int J Climatol 34:3986–3997

Kim EJ, Hong SY (2010) Impact of air-sea interaction on East Asian summer monsoon climate in WRF. J Geophys Res Atmos 115:D19118. https://doi.org/10.1029/2009JD013253

Koo MS, Hong SY (2010) Diurnal variations of simulated precipitation over East Asia in two regional climate models. J Geophys Res Atmos 115:D05105. https://doi.org/10.1029/2009JD012574

Lau KM, Yang GJ, Shen SH (1988) Seasonal and intraseasonal climatology of summer monsoon rainfall over East Asia. Mon Weather Rev 116:18–37. https://doi.org/10.1175/1520-0493(1988)116%3c0018:saicos%3e2.0.co;2

Leung LR, Yun Q, Bian X, Washington WM, Han J, Roads JO (2004) Mid-century ensemble regional climate change scenarios for the Western United States. Clim Change 62:75–113

Li P, Furtado K, Zhou T, Chen H, Li J, Guo Z, Xiao C (2018) The diurnal cycle of East Asian summer monsoon precipitation simulated by the Met Office Unified Model at convection-permitting scales. Clim Dyn. https://doi.org/10.1007/s00382-018-4368-z

Liang XZ, Li L, Dai A, Kunkel KE (2004a) Regional climate model simulation of summer precipitation diurnal cycle over the United States. Geophys Res Lett 31:357–370

Liang XZ, Li L, Kunkel KE, Ting M, Wang JX (2004b) Regional climate model simulation of U.S. precipitation during 1982–2002. Part I: annual cycle. J Clim 17:3510–3529. https://doi.org/10.1175/1520-0442(2004)017%3c3510:RCMSOU%3e2.0.CO;2

Lim K-SS, Hong S-Y (2010) Development of an effective double-moment cloud microphysics scheme with prognostic cloud condensation nuclei (CCN) for weather and climate models. Mon Weather Rev 138:1587–1612. https://doi.org/10.1175/2009mwr2968.1

Ma L-M, Tan Z-M (2009) Improving the behavior of the cumulus parameterization for tropical cyclone prediction: convection trigger. Atmos Res 92:190–211. https://doi.org/10.1016/j.atmosres.2008.09.022

Neupane N, Cook KH (2013) A nonlinear response of sahel rainfall to atlantic warming. J Clim 26:7080–7096. https://doi.org/10.1175/jcli-d-12-00475.1

Niu X et al (2015a) Multi-model ensemble projection of precipitation in eastern China under A1B emission scenario. J Geophys Res Atmos 120:9965–9980

Niu X et al (2015b) Projection of Indian summer monsoon climate in 2041–2060 by multi-regional and global climate models. J Geophys Res Atmos 120:1776–1793

Pei L, Moore N, Zhong S, Luo L, Hyndman DW, Heilman WE, Gao Z (2014) WRF model sensitivity to land surface model and cumulus parameterization under short-term climate extremes over the Southern Great Plains of the United States. J Clim 27:7703–7724

Pohl B, Rouault M, Roy SS (2014) Simulation of the annual and diurnal cycles of rainfall over South Africa by a regional climate model. Clim Dyn 43:2207–2226

Pu B, Cook KH (2012) Role of the West African Westerly Jet in Sahel Rainfall Variations. J Clim 25:2880–2896. https://doi.org/10.1175/jcli-d-11-00394.1

Qiao F, Liang XZ (2015) Effects of cumulus parameterizations on predictions of summer flood in the Central United States. Clim Dyn 45:727–744

Qiao F, Liang XZ (2016) Effects of cumulus parameterization closures on simulations of summer precipitation over the United States coastal oceans. J Adv Model Earth Syst 8:764–785. https://doi.org/10.1002/2015MS000621

Reynolds RW, Smith TM (1994) Improved global sea surface temperature analyses using optimum interpolation. J Clim 7:929–948. https://doi.org/10.1175/1520-0442(1994)007%3c0929:igssta%3e2.0.co;2

Shen W, Tang J, Wang Y, Wang S, Niu X (2017) Evaluation of WRF model simulations of tropical cyclones in the western North Pacific over the CORDEX East Asia domain. Clim Dyn 48:2419–2435. https://doi.org/10.1007/s00382-016-3213-5

Skamarock WC, Klemp JB (2008) A time-split nonhydrostatic atmospheric model for weather research and forecasting applications. J Comput Phys 227:3465–3485

Sun X, Ming X, Brotzge J, Mcpherson RA, Hu XM, Yang XQ (2016a) An evaluation of dynamical downscaling of central plains summer precipitation using a WRF-based regional climate model at a convection-permitting 4 km resolution: dynamical downscaling at CP resolution. J Geophys Res Atmos 121:13801–13825. https://doi.org/10.1002/2016JD024796

Sun X, Jiang G, Ren X, Yang XQ (2016b) Role of intraseasonal oscillation in the persistent extreme precipitation over the Yangtze River Basin during June 1998. J Geophys Res Atmos 121:10453–10469. https://doi.org/10.1002/2016JD025077

Sun X, Xu Y, Zhang Z, Yang XQ (2019) The tropical and extra-tropical-origin summer meridional teleconnections over East Asia. Clim Dyn 53:721–735. https://doi.org/10.1007/s00382-018-04610-2

Tang J, Wang S, Niu X, Hui P, Zong P, Wang X (2017) Impact of spectral nudging on regional climate simulation over CORDEX East Asia using WRF. Clim Dyn 48:2339–2357. https://doi.org/10.1007/s00382-016-3208-2

Tang J, Sun X, Hui P, Li Y, Zhang Q, Liu J (2018) Effects of spectral nudging on precipitation extremes and diurnal cycle over CORDEX-East Asia domain. Int J Climatol 38:4903–4923. https://doi.org/10.1002/joc.5706

Walther A, Jeong J-H, Nikulin G, Jones C, Chen D (2013) Evaluation of the warm season diurnal cycle of precipitation over Sweden simulated by the Rossby Centre regional climate model RCA3. Atmos Res 119:131–139. https://doi.org/10.1016/j.atmosres.2011.10.012

Wang P, Tang J, Sun X, Liu J, Juan F (2018) Spatiotemporal characteristics of heat waves over China in regional climate simulations within the CORDEX-EA project. Clim Dyn. https://doi.org/10.1007/s00382-018-4167-6

Wang P, Hui P, Xue D, Tang J (2019) Future projection of heat waves over China under global warming within the CORDEX-EA-II project. Clim Dyn. https://doi.org/10.1007/s00382-019-04621-7

Xu W (2013) Precipitation and convective characteristics of summer deep convection over East Asia observed by TRMM. Mon Weather Rev 141:1577–1592

Yang B, Zhou Y, Zhang Y, Huang A, Qian Y, Zhang L (2018) Simulated precipitation diurnal cycles over East Asia using different CAPE-based convective closure schemes in WRF model. Clim Dyn 50:1639–1658. https://doi.org/10.1007/s00382-017-3712-z

Yang L, Wang S, Tang J, Niu X, Fu C (2019) Evaluation of the effects of a multiphysics ensemble on the simulation of an extremely hot summer in 2003 over the CORDEX-EA-II region. Int J Climatol 39:3413–3430. https://doi.org/10.1002/joc.6028

Yin S, Chen D, Xie Y (2009) Diurnal variations of precipitation during the warm season over China. Int J Climatol 29:1154–1170. https://doi.org/10.1002/joc.1758

Yu R, Zhou T, Xiong A, Zhu Y, Li J (2007) Diurnal variation of summer precipitation over contiguous China. Geophys Res Lett 34:223–234

Yuan W, Lin W, Yu R, Zhang M, Chen H, Li J (2012) Regimes of diurnal variation of summer rainfall over subtropical East Asia. J Clim 25:3307–3320

Yuan W, Yu R, Zhang M, Lin W, Jian L, Fu Y (2013) Diurnal cycle of summer precipitation over subtropical East Asia in CAM5. J Clim 26:3159–3172

Zhang Y, Chen H (2015) Comparing CAM5 and superparameterized CAM5 simulations of summer precipitation characteristics over Continental East Asia: mean state, frequency-intensity relationship, diurnal cycle, and influencing factors. J Clim 29:1067–1089. https://doi.org/10.1175/JCLI-D-15-0342.1

Zhang Y, Chen H (2016) Comparing CAM5 and super parameterized CAM5 simulations of summer precipitation characteristics over continental East Asia: mean state, frequency-intensity relationship, diurnal cycle, and influencing factors. J Clim 29(3):1067–1089. https://doi.org/10.1175/JCLI-D-15-0342.1

Zheng Y, Alapaty K, Herwehe JA, Genio ADD, Niyogi D (2016) Improving high-resolution weather forecasts using the weather research and forecasting (WRF) model with an updated kain-fritsch scheme. Mon Weather Rev 144:833–860. https://doi.org/10.1175/mwr-d-15-0005.1

Zhou T-J, Yu R-C (2005) Atmospheric water vapor transport associated with typical anomalous summer rainfall patterns in China. J Geophys Res Atmos 110:D08104. https://doi.org/10.1029/2004JD005413

Zhou T, Yu R, Chen H, Dai A, Pan Y (2008) Summer precipitation frequency, intensity, and diurnal cycle over China: a comparison of satellite data with rain gauge observations. J Clim 21:3997–4010. https://doi.org/10.1175/2008jcli2028.1

Zou L, Zhou T (2013) Improve the simulation of western North Pacific summer monsoon in RegCM3 by suppressing convection. Meteorol Atmos Phys 121:29–38. https://doi.org/10.1007/s00703-013-0255-7

Zou L, Zhou T (2014) Simulation of the western North Pacific summer monsoon by regional ocean–atmosphere coupled model: impacts of oceanic components. Chin Sci Bull 59:662–673. https://doi.org/10.1007/s11434-013-0104-6

Zou L, Zhou T (2016) Future summer precipitation changes over CORDEX-East Asia domain downscaled by a regional ocean-atmosphere coupled model: a comparison to the stand-alone RCM. J Geophys Res 121:2691–2704